JES Focus Issue on Advances in Electrochemical Processes for Interconnect Fabrication in Integrated Circuits

In-Situ Stress Measurements during Cobalt Electrodeposition

V. P. Graciano, U. Bertocci,* and G. R. Stafford *,z

Material Measurement Laboratory, National Institute of Standards and Technology, Gaithersburg, Maryland 20899, USA

In situ cantilever curvature is used to quantify the growth stress in Co thin films, electrodeposited from an electrolyte consisting of 0.5 mol/L Na_2SO_4, 0.5 mol/L H_3BO_3, and 0.1 mol/L $CoSO_4 \cdot 7\ H_20$. The average biaxial steady-state stress is measured as a function of the deposition potential and is examined as a function of growth rate. Stresses as low as +85 MPa (tensile) are obtained at small growth rate, increasing to a limiting value of 800 MPa as the growth rate is increased. The data is fit to a kinetic model that appears in the literature and treats the stress as a dynamic competition between coalescence-induced tensile stress and compressive stress due to insertion of atoms into the grain boundary. Kinetic parameters for Co indicate that stress development is dominated by nuclei coalescence and that ad-atom insertion into the grain boundary contributes to the overall stress only at very low growth rates.
© The Author(s) 2019. Published by ECS. This is an open access article distributed under the terms of the Creative Commons Attribution 4.0 License (CC BY, http://creativecommons.org/licenses/by/4.0/), which permits unrestricted reuse of the work in any medium, provided the original work is properly cited. [DOI: 10.1149/2.0311901jes]

Manuscript submitted November 21, 2018; revised manuscript received December 28, 2018. Published January 12, 2019. *This paper is part of the JES Focus Issue on Advances in Electrochemical Processes for Interconnect Fabrication in Integrated Circuits.*

Co-based thin films have attracted much attention over the past several decades due in part to their interesting magnetic,[1–3] mechanical,[4–6] and catalytic properties.[7–10] More recently, Co has made inroads in microelectronics, specifically on-chip metallization, serving as a capping layer for Cu to suppress electromigration.[11] Co is also being considered as a possible replacement for electrolytic Cu due to the fact that Co outperforms Cu for line widths less than 15 nm.[12,13] Although much focus has been on electroless Co, the deposition of high purity metal required by industry may be challenging for electroless processes unless appropriate chemical reducing agents can be developed. Superconformal filling of submicron features has been demonstrated using electrolytic Co. Void-free filling can be achieved through the use of organic inhibitors that influence local deposition rates through competitive adsorption/deactivation without degrading the desired properties.[14,15]

Regardless of the deposition method, thin films usually develop significant stress which can have a major influence on the reliability and lifetime of the film.[16–23] In interconnects, stress is usually detrimental to device performance and has been associated with electromigration, morphology and resistance changes, corrosion, and other failure mechanisms.[24] As a consequence, a good understanding of the origin and development of stress during film deposition is important. The evolution of residual stress during thin film growth depends on several factors including deposit microstructure, growth conditions, and properties of the material being deposited. Tensile stress generally dominates the early stages of film growth as discrete nuclei coalesce into a continuous film.[17] However, as films become thicker and more uniform in height, the stress often reaches a constant steady-state value. High mobility materials tend to generate compressive stress when deposited at high temperature or low growth rates, resulting in the compressive-tensile-compressive (CTC) stress transitions that are typically observed for high-mobility Volmer-Weber growth. CTC behavior is attributed to the nucleation of 3-D islands, their coalescence, and finally their thickening as a continuous film.[17] Alternatively, the growth of low mobility materials tends to produce films with large tensile stresses when deposited at low temperature or at high growth rates. However, for a given material that develops tensile stress under one set of growth conditions, compressive stress can develop under a different set of conditions. For example, the influence of growth rate on steady-state stress has been nicely demonstrated in Ni electrodeposited from surfactant-free sulfamate electrolyte.[18] The stress was shown to vary from −500 MPa to +500 MPa as the growth rate (current density) was increased while the grain structure remained the same. Similar results have also been reported for electrodeposited Cu from additive-free acidic sulfate electrolyte.[25]

There is general agreement in the literature that the final steady-state stress is determined by competing processes that simultaneously generate both tensile and compressive stress. In the earliest stages of deposition, tensile stress is generated when individual nuclei coalesce to form a continuous film.[20,22,26–28] Because the surface energy of the nuclei is larger than the free energy of the grain boundary that is formed, the system energy can be reduced if the individual nuclei coalesce into a continuous film. The reduction of surface energy is balanced by an increase of elastic strain energy which gives rise to tensile stress in the film. This tensile stress is maintained as the film thickens and the grain boundary length increases. Understanding the exact mechanisms that generate the compressive stress is still an active area of research.[23,29–32] Chason has proposed a grain boundary insertion mechanism where compressive stress is generated by the diffusion of atoms into the grain boundary as the film grows.[30] The driving force is the non-equilibrium conditions on the surface during deposition that lead to an increase in the chemical potential of adatoms relative to equilibrium conditions. This mechanism accounts for both residual compressive stress in the film and the observed relaxation of compressive stress when deposition is interrupted.[30,33] Additional models based on this grain boundary insertion mechanism have been developed.[34–36]

Chason's model treats steady-state stress as a dynamic competition between tensile and compressive stress generation mechanisms that are largely governed by atomic mobility, microstructure, and deposition rate.[37–39] The resulting rate equations describe the balance between tensile stress due to grain coalescence and compressive stress due to insertion of atoms into the grain boundary and mediated by transport of atoms from the surface. They also capture the experimentally observed dependence of the steady-state stress on the growth rate. At high growth rate, tensile stress due to coalescence dominates as the rate of adatom insertion into the grain boundary is small compared to the overall increase in film thickness. In contrast, at low growth rate, the grain boundary length increases rather slowly, allowing sufficient time for adatoms to enter the grain boundary, thereby generating compressive stress. The stress is mediated by the rate at which the grain boundary grows relative to the rate of insertion of atoms into the grain boundary. This model has properly captured the growth rate dependence for both electrodeposited Ni and Cu.[37–40] More recent versions of the model also consider deposit microstructure and grain growth.[41–43]

Stress development in electrodeposited Co has only been superficially examined. Cammarata[44] has reported that Co galvanostatically

*Electrochemical Society Fellow.
[z]E-mail: gery.stafford@nist.gov

Downloaded on 2019-01-15 to IP 108.31.232.242 address. Redistribution subject to ECS terms of use (see ecsdl.org/site/terms_use) unless CC License in place (see abstract).

electrodeposited onto amorphous NiTi shows CTC stress transitions that are typically observed for high-mobility Volmer-Weber growth.[17] However, only a single current density was examined. Stress measurements during the initial stages of Co deposition onto (111)-textured Au from very dilute Co^{2+} solutions have also been reported.[45] Due to the low current efficiency and co-generation of hydrogen, these films developed the face-centered cubic structure rather than the hexagonal close-packed structure of pure Co. To the best of our knowledge, no in-depth analysis of stress development during Co electrodeposition from more concentrated Co^{2+} electrolytes appears in the literature. In this paper, we use in situ wafer curvature to measure the stress that develops in 50 nm thick Co films electrodeposited from Na_2SO_4 – based electrolyte. We have measured the biaxial steady-state stress as a function of overpotential and observe a significant increase in tensile stress at more negative deposition potential. When examined as a function of growth rate, the steady-state stress increase is consistent with Chason's kinetic model. Kinetic parameters obtained from the model are compared to literature values for electrodeposited Cu and Ni, and the significance of their differences is discussed.

Experimental

In situ stress measurements were made on a vibration-isolating optical bench using the cantilever bending method. The cantilever was a borosilicate glass (Schott North America, Inc.[a]) strip measuring 60 mm × 3 mm × 0.108 mm. The Young's modulus and Poisson ratio of the glass cantilever were 72.9×10^9 N/m^2 and 0.208, respectively. A 5 nm thick adhesion layer of titanium (Ti) and a subsequent 250 nm film of gold (Au) were vapor-deposited onto one side of the cantilever by electron-beam evaporation. The Au electrode had a (111) crystallographic orientation. The curvature of the substrate was monitored while in the electrolyte and under potential control by reflecting a HeNe laser off of the glass/metal interface onto a position-sensitive detector (PSD). A more detailed description of the optical bench is published elsewhere.[25,46]

The relationship between the force per cantilever beam width, $\boldsymbol{F_w}$, exerted by processes occurring on the electrode surface and the curvature induced in the cantilever (κ) is given by Stoney's equation[47]

$$F_w = \bar{\sigma} h_f = \frac{\mathrm{E} h_s^2\, \kappa}{6\,(1-\nu)} \qquad [1]$$

where $\boldsymbol{E}$, $\boldsymbol{\nu}$, and $\boldsymbol{h_s}$ are the Young's modulus, Poisson ratio, and thickness of the glass substrate respectively. For metal deposition, $\boldsymbol{F_w}$ is equal to the stress-thickness product, $\bar{\sigma} h_f$, the average biaxial film stress ($\bar{\sigma}$) multiplied by the thickness of the film ($\boldsymbol{h_f}$). A single stationary laser measures only the change in curvature, rather than absolute curvature, by measuring the deflection of the cantilever. A small angle approximation was used to estimate the curvature of the glass cantilever directly from the reflected laser position on the PSD.[25] The initial value of $\bar{\sigma} h_f$ is arbitrarily set to zero at the beginning of the measurement. Because the stress in polycrystalline films is generally not uniform through its thickness, $\bar{\sigma} h_f$ can be calculated by integrating the thickness-dependent in-plane stress distribution ($\boldsymbol{\sigma}$ $(\boldsymbol{z,t})$) over the thickness of the film:

$$\bar{\sigma} h_f = \int_0^{h_f} \sigma\,(z,t)\; dz \qquad [2]$$

Throughout this paper, we will refer to $\bar{\sigma} h_f$ as the stress-thickness. It is measured in real-time by monitoring the cantilever deflection during Co deposition and stripping.

The electrolyte was 0.5 mol/L Na_2SO_4 (Mallinckrodt, AR) + 0.5 mol/L H_3BO_3 (Mallinckrodt, AR) + 0.1 mol/L $CoSO_4 \cdot 7\ H_20$ (Aldrich) and was prepared using 18.3 MΩ-cm ultrapure water (Barnstead). The pH of the solution was 4.5. The electrochemical cell was a single-compartment borosilicate cell covered by a polytetrafluoroethylene cap. A glass disk was joined to the back of the cell to allow it to be held and positioned by a standard mirror mount on the optical bench. The electrode holder that clamped the top of the cantilever electrode was positioned so that the entire length of cantilever contributing to the curvature was electrochemically active. A typical immersion length was 22 mm, leading to an exposed area of 0.66 cm^2. The counter electrode was a spiraled Co wire placed parallel to and in the same solution as the working electrode. The reference electrode was a saturated mercury-mercurous sulfate electrode (SSE) that was separated from the working compartment by a Vycor-tipped bridge filled with 0.5 mol/L Na_2SO_4. All potentials are referenced to the SSE. The electrolyte was initially purged with ultra-pure argon, and gas flow was maintained in the headspace throughout the experiment. Potential control was maintained using an EG&G Princeton Applied Research Corp. (PARC) model 273 potentiostat-galvanostat controlled by a Dell Pentium 4 computer and LabView software. All measurements were made at room temperature.

An electrochemical quartz crystal microbalance (EQCM, Maxtek Inc.) was employed to measure mass changes during Co deposition and stripping in order to quantify the current efficiency. The quartz crystals were polished 2.54 cm AT cut disks with a 5 MHz resonant frequency. Titanium and Au were vapor deposited onto the quartz crystals by the manufacturer. The glass cell for the EQCM measurements had separate compartments for the working, counter, and SSE reference electrodes. Before introduction into the cell, the solution was thoroughly de-aerated by bubbling high purity Ar, and flow was maintained in the headspace of the cell during measurements. The EQCM measures both the resonant frequency and the resistance R_1 of the equivalent resonant circuit. The value of R_1 in all measurements changed very little, confirming that no significant roughening of the electrode surface occurred during deposition.

In order to characterize the post-deposition structure and surface morphology, Co was electrodeposited onto (111) Si wafers with 5 nm of Ti and 250 nm of Au deposited by electron-beam evaporation. The Au surface was masked to expose an area of 0.13 cm^2. These deposits were examined by X-ray diffraction using a Siemens D-500 diffractometer with Cu-Kα radiation and by scanning electron microscopy (SEM) using a JEOL JSM-7100 FE-SEM with an accelerating voltage of 5 kV and a working distance of 8–10 mm. We report an average grain size (and standard deviation) based on at least 75 measurements taken from plane-view micrographs.

Results and Discussion

Potentiodynamic behavior.—Figure 1 shows the voltammetric (red) and stress-thickness (blue) response of a Au cantilever electrode in 0.5 mol/L Na_2SO_4 + 0.5 mol/L H_3BO_3 containing 0.1 mol/L $CoSO_4$ at a pH of 4.5. The black curve is the voltammetric response in the absence of $CoSO_4$. The onset of Co deposition is clearly observed near −1.2 V. The increase in cathodic current on the return sweep is an indication that a nucleation overpotential is required to electrodeposit Co onto Au. The return sweep also shows the electrochemical dissolution of Co from the Au surface at potentials positive of −1.0 V. This stripping wave is featureless; the additional stripping wave(s) typically associated with hydrogen incorporation into Fe-group metals is absent.[48]

The stress moves in the tensile (positive) direction from a value arbitrarily chosen as 0 as the potential is swept in the cathodic direction. Prior to Co deposition, the overall stress change is about +0.4 N/m. This tensile response reflects the change in the surface charge density caused by the change in potential or by the desorption of $SO_4{}^{2-}$ from the Au surface. This stress change is consistent with Ibach's adsorbate-induced stress model in which electron acceptors such as adsorbed anions (e.g., $SO_4{}^{2-}$) cause compressive stress because they reduce the electron density in the surface.[49] As a consequence, their desorption from the surface results in net tensile stress. At the onset of Co deposition, the tensile stress increases sharply and continues to increase even during the return sweep, as Co continues to deposit,

[a]Certain trade names are mentioned for experimental information only; in no case does it imply a recommendation or endorsement by NIST.

Downloaded on 2019-01-15 to IP 108.31.232.242 address. Redistribution subject to ECS terms of use (see ecsdl.org/site/terms_use) unless CC License in place (see abstract).

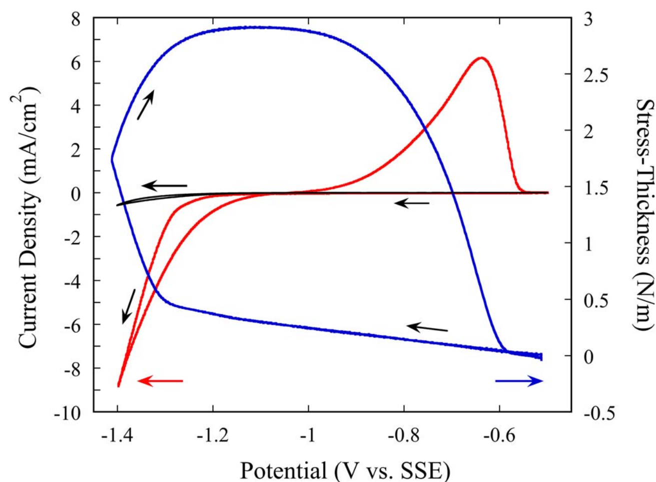

Figure 1. Potentiodynamic scan (red) and stress-thickness response (blue) of (111)-textured Au cantilever electrode in 0.1 mol/L $CoSO_4$ + 0.5 mol/L H_3BO_3 + 0.5 mol/L Na_2SO_4 and sweep rate of 100 mV/s. The black line is the voltammetric response in the absence of $CoSO_4$. The solution pH was 4.5.

before reaching a nearly constant value. The stress begins to decrease at the onset of Co dissolution. After the film is completely stripped, the stress returns to its initial zero value.

Although not readily apparent from the voltammetry in Fig. 1, the faradaic efficiency for Co deposition is less than 100%. In pH 4.5 solution, hydronium ion reduction occurs at about −1.0 V (not visible), followed by H_2O reduction at about −1.3 V, as seen in the Co^{2+}-free voltammetry in Fig. 1. The consequence of these side reactions is the possible precipitation of $Co(OH)_2$ due to a local increase in pH at the electrode surface. The reported K_{sp} of $Co(OH)_2$ is 1.09×10^{-15}.[50] We estimate that a pH of 7 is required to precipitate $Co(OH)_2$ from a solution containing 0.1 mol/L Co^{2+} (see Supplemental Information for derivation). This pH value can clearly be achieved at potentials negative of H_2O reduction where OH^- is generated during H_2 evolution,[51–53] although H_3BO_3 may serve as a buffer or its reduction may compete with that of H_2O as a side reaction that does not influence the pH.[54] $Co(OH)_2$ may also be precipitated at more positive potentials (≈−1.2 V) in which hydronium is reduced but the surface concentration of Co^{2+} remains close to the bulk value, as discussed in more detail in a later section of the paper.

Single pulse deposition.—Figure 2 shows the current (**a**) and stress-thickness (**b**) response for potential steps into the Co deposition region, followed by a 2 mV/s potentiodynamic scan to strip the Co deposit from the Au surface. The electrode was equilibrated at the open circuit potential (≈ −1.05 V) for 10 s prior to initiating the potentiodynamic scan. The inset in (**a**) shows an example of how the applied potential varied with time. The duration of each deposition pulse was sufficient to deposit a 50 nm Co film, assuming 100% current efficiency. Following double layer charging (Fig. 2a), the deposition current increases, reaches a maximum, and then decreases for E ≤ −1.275 V or remains constant for E ≥ −1.25 V. The maximum current increases while the time to reach the peak current decreases at more negative deposition potentials. Both of these features of the current response suggest an increase in nucleation density and are consistent with nucleation and diffusion-controlled growth models that appear in the literature.[55] The stripping current shape and magnitude are similar to those in the Fig. 1 voltammetric measurement. The peak currents are about the same for deposits formed at the more negative potentials, indicating that the deposit thicknesses are similar. For deposition potentials more positive than −1.25 V, the stripping current decreases, suggesting a decrease in faradaic efficiency. In addition, the dissolution current for the film deposited at the most positive potential (−1.190 V) shows a second peak following the primary stripping

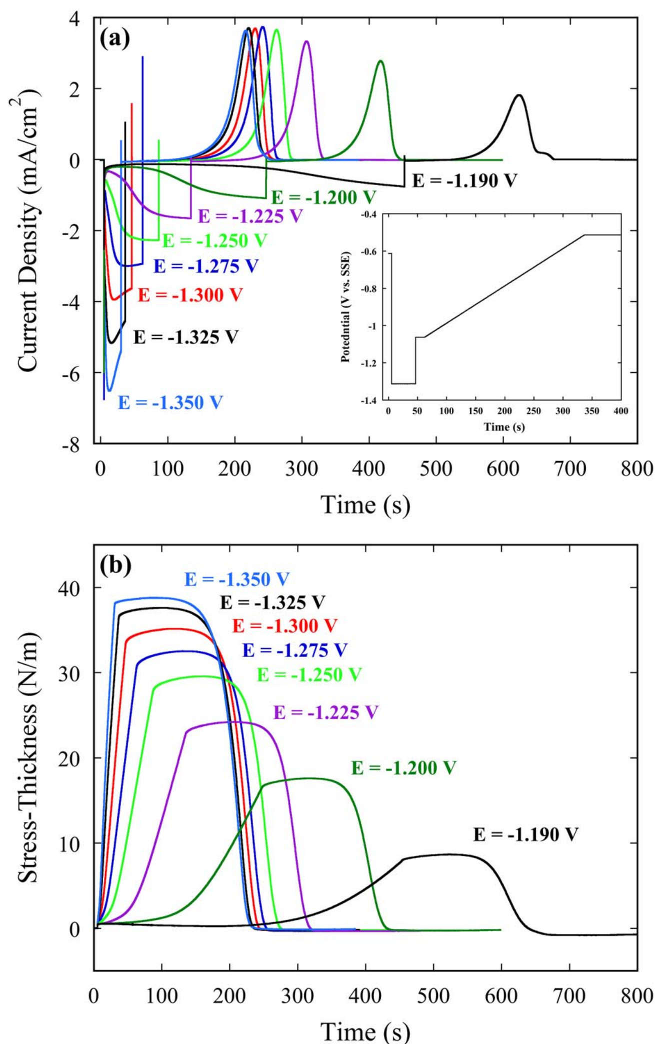

Figure 2. (a) Chronoamperometry and (b) stress-thickness response for Co electrodeposition onto a Au cantilever electrode in 0.1 mol/L $CoSO_4$ + 0.5 mol/L H_3BO_3 + 0.5 mol/L Na_2SO_4 (pH 4.5). The potential was stepped from −0.6 V to the deposition potential of interest for a nominal deposit thickness of 50 nm while the cantilever deflection was monitored by the PSD. Following deposition, the electrode was allowed to equilibrate at the open circuit potential (≈ −1.05 V) for 10 s prior to initiating an anodic voltammetric sweep at 2 mV/s until the deposit was completely removed. The stripping potential was limited to −0.5V. The inset in (a) shows an example of how the applied potential varied with time.

peak, suggesting that Co dissolution is hindered, perhaps by the precipitation of $Co(OH)_2$. The fact that none of the other deposits show this additional stripping peak allows us to conclude that any possible $Co(OH)_2$ precipitation occurs during Co deposition, not dissolution.

We show a similar series of deposition-stripping experiments using the EQCM in Fig. S1 of the Supporting Information. The deposit thicknesses vary from 40 to 130 nm. The lag time for Co deposition is quite evident at the more positive deposition potentials, whereas for the more negative potentials, deposition begins quite rapidly. Following stripping, the mass returns to zero, indicating that all of the Co is removed. There is also no evidence for a $Co(OH)_2$ precipitate remaining on the surface following Co stripping. Fig. S1(b) is a plot of the mass converted to thickness for the first 50 nm of deposition. The EQCM data indicate that the Co deposition rate is at steady-state by the time the deposit thickness reaches 50 nm. Interestingly, neither the EQCM deposition currents (not shown) nor the deposition currents shown in Fig. 2a from the stress bench have reached steady-state for the more negative deposition potentials, suggesting that the decrease

Downloaded on 2019-01-15 to IP 108.31.232.242 address. Redistribution subject to ECS terms of use (see ecsdl.org/site/terms_use) unless CC License in place (see abstract).

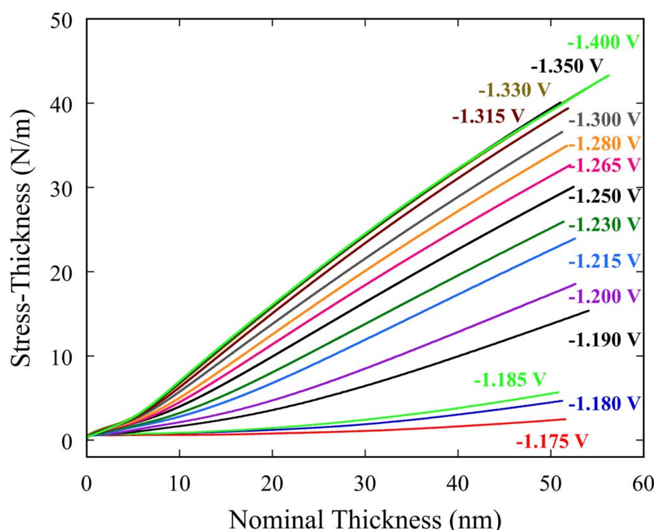

Figure 3. Evolution of stress-thickness product vs. nominal deposit thickness associated with the chronoamperometry curves shown in Figure 2. The deposit thickness was determined from the cathodic charge density assuming a Co current efficiency of 100%.

in current may have contributions from parasitic reactions rather than simply Co deposition.

The Fig. 2b stress-thickness response is tensile for all deposition potentials. The magnitude of the stress as well as its time derivative increase significantly as the deposition potential is made more negative. The stress plateau following deposition and prior to stripping indicates that stress relaxation is not significant under these deposition conditions. The stable growth stress also suggests that the deposit structure, particularly the grain size, does not change significantly over this time period. The stress-thickness response shows the same reversibility as the chronoamperometry, decreasing during stripping and returning to its initial zero value. It should be noted that the final stress-thickness value for deposits formed at small overpotential (−1.190 V) is slightly compressive. Although this might suggest that $Co(OH)_2$ remains on the surface as a precipitate, such a conclusion is not supported by EQCM measurements at the same potential.

We now examine the stress-thickness changes observed during Co deposition in more detail. The rate of change of the stress-thickness can be expressed as

$$\frac{d\left(\bar{\sigma}h_f\right)}{dt} = \sigma\left(h_f\right)\frac{\partial h_f}{\partial t} + \int_0^{h_f}\frac{\partial\sigma(z,t)}{\partial t}dz \qquad [3]$$

The two terms on the right side of the equation capture the different ways in which the stress-thickness can change. The first term corresponds to changes in the film thickness, adding new layers to the surface of the film (at $z = \boldsymbol{h_f}$) with a biaxial stress of $\boldsymbol{\sigma}(\boldsymbol{h_f})$. We refer to this as the incremental stress since it corresponds to the deposition of new layers under stress. The second term on the right side captures any relaxation processes that might occur in material that has already been deposited. The stress term in the integral expression of Eq. 3 has a dependence on both thickness and time. If the stress in the film does not change once it has been deposited, then the second term in Eq. 3 is zero and the incremental stress can be obtained from the slope of the stress-thickness plotted as a function of the deposit thickness:[37]

$$\sigma\left(h_f\right) = \frac{d\left(\bar{\sigma}h_f\right)/dt}{dh_f/dt} = \frac{d\left(\bar{\sigma}h_f\right)}{dh} \qquad [4]$$

Figure 3 shows the stress-thickness response for a range of deposition potentials plotted as a function of the nominal deposit thickness, assuming 100% current efficiency for Co deposition. All of the stress-thickness vs. thickness curves eventually become linear with slopes that increase as the deposition potential is made more negative. If we assume that no stress relaxation occurs in the underlying layers, then the slope of these curves represents the stress in the layer being added to the deposit at thickness $\boldsymbol{h_f}$ (Eq. 4). We define the steady-state region, in which $\boldsymbol{\sigma}(\boldsymbol{h_f})$ reaches a constant value, as the steady-state stress ($\boldsymbol{\sigma_{ss}}$). The assumption that no stress relaxation occurs in the underlying layers is likely a valid assumption, based on the nearly constant stress values observed at open circuit following deposition in Fig. 2b. To examine this further, we refer to Fig. S2 of the Supporting Information. Figure S2(a) shows the stress-thickness plotted as a function of the nominal deposit thickness for Co deposits approximately 300 nm in thickness. The curves are reasonably similar to those shown in Fig. 3. Figure S2(b) shows the stress-thickness for the same deposits in S2(a) plotted as a function of the nominal deposit thickness but measured during the electrochemical dissolution of the Co deposits. The curves obtained during deposition and dissolution are nearly identical, a clear indication that the stress throughout the deposits is quite stable. This validates our use of Eq. 4 to obtain the steady-state stress.

Quartz crystal nanobalance.—The stress-thickness curves shown in Fig. 3 are plotted with respect the nominal deposit thickness. In order to obtain an accurate value for the steady-state stress, the stress-thickness needs to be plotted with respect to the actual deposit thickness by considering the deposition current efficiency. Although stripping voltammetry like that shown in Fig. 2a can provide the average current efficiency for the entire deposit, this number may not accurately depict the efficiency in the latter stages of deposition where the stress reaches steady state. The EQCM allows us to measure both the mass change and the total charge during Co deposition onto a Au-coated quartz crystal. The figure of merit is the mass-charge coefficient (d**m**/d**q**) which has units of mg/C. The expected value of d**m**/d**q** for Co deposition, assuming 100% current efficiency, is −0.30 mg/C. Figure 4a is a plot of the measured d**m**/d**q** as a function of deposition time for the mass data shown in Fig. S1. At small overpotentials, Co deposition is inhibited in the early stages. For deposition at −1.190 V, no mass increase is observed for the first 300 s. This inhibition time decreases significantly as the deposition potential is made more negative. For potentials negative of −1.225 V, the steady-state d**m**/d**q** converges to a value of about −0.26 mg/C, or about an 87% current efficiency. In addition to the previously mentioned inhibition, deposition at −1.190 V has a d**m**/d**q** that exceeds the −0.30 mg/C theoretical value. The expected value of d**m**/d**q** for $Co(OH)_2$ precipitation is −0.48 mg/C, in which it is assumed that the charge associated with $Co(OH)_2$ precipitation is the reduction of $2H^+$. A d**m**/d**q** that exceeds −0.30 mg/C is a clear indication that $Co(OH)_2$ is precipitated along with Co deposition.[56] Because Co deposition is inhibited in the early stages of deposition, the surface concentration of Co^{2+} remains near the bulk value of 0.1 mol/L. At these potentials and pH, H_3O^+ is reduced at the mass transport limit, resulting in a local pH increase, sufficient to precipitate $Co(OH)_2$ on the surface and possibly interfere with the Co^{2+} aquo-complex reduction.

It is also interesting to note the difference between the steady-state current efficiency and the average current efficiency obtained by stripping voltammetry. These are plotted in Fig. 4b. The steady-state current efficiency is greater than 83% and slightly increases at more negative potentials. In contrast, the average current efficiency is above 80% only at potentials more negative than −1.25 V. The additional time required to nucleate and grow Co at the more positive deposition potentials results in very low current efficiencies. This deposition delay may in part be due to the precipitation of $Co(OH)_2$, although our data do not directly show that this is the case. The lower current efficiencies could simply reflect the large nucleation overpotential required to deposit Co onto the Au surface.

Steady-state stress.—Because the current efficiency for Co deposition is a function of both time and potential, accurately correcting the thickness values in Fig. 3 to obtain stress-thickness curves based on the actual deposit thickness is not possible. However, the steady-state stress can be quantitatively obtained from the slopes in the steady-state

Downloaded on 2019-01-15 to IP 108.31.232.242 address. Redistribution subject to ECS terms of use (see ecsdl.org/site/terms_use) unless CC License in place (see abstract).

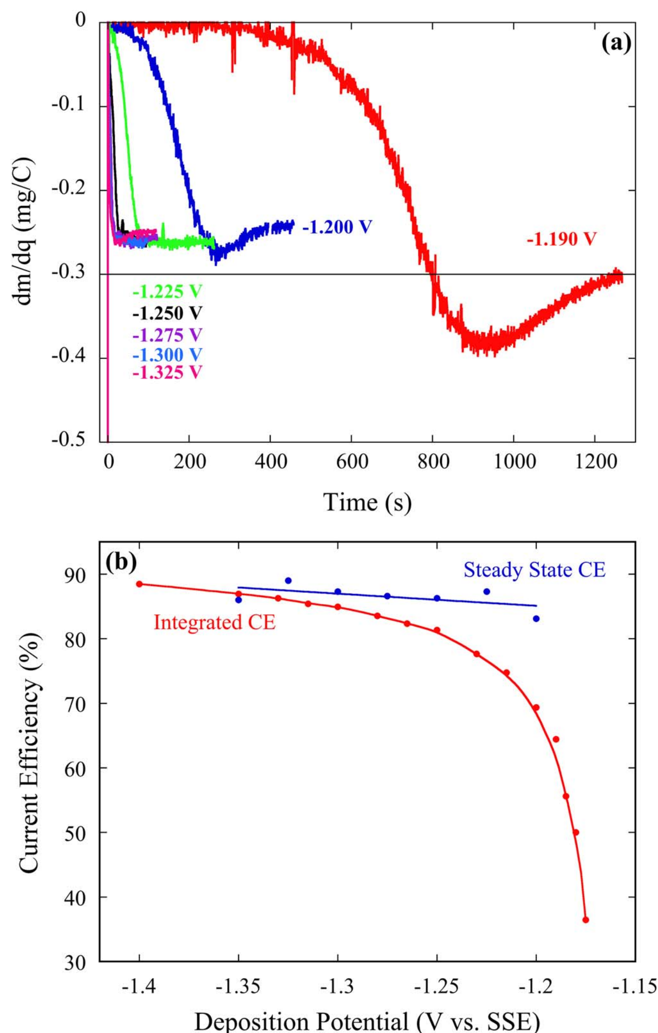

Figure 4. (a) EQCM mass-charge ratios (mg/C) plotted as a function of deposition time for the deposition potentials shown in the figure. (b) Co current efficiency plotted as a function of deposition potential. The data in blue is the steady-state current efficiency determined from the final d$\boldsymbol{m}$/d$\boldsymbol{q}$ values shown in (a) and normalized to the theoretical value of −0.3 mg/C. The data in red is the average current efficiency calculated by dividing the stripping charge by the total deposition charge that was obtained from the chronoamperometry curves in Fig. 2a.

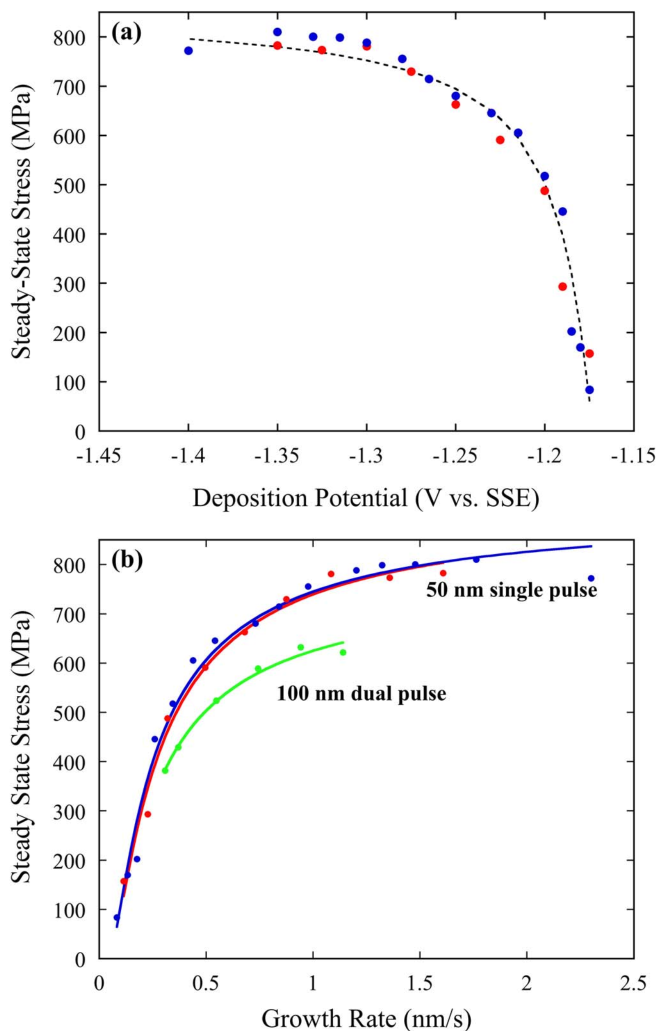

Figure 5. Steady-state stress of electrodeposited Co thin films plotted as a function of (a) deposition potential and (b) growth rate. The growth rate was determined from Eq. 5, using the average current density measured over the last 5 nm of deposition. The data in (a) consists of two independent data sets, each using a single pulse at each deposition potential. The thickness was limited to 50 nm. The dashed line is simply a guide for the eye. The data in (b) consists of the two data sets in (a) plus data from 100 nm thick deposits that were grown using a dual pulse; a nucleation pulse to −1.30 V for 15 nm, followed by a growth pulse to the desired deposition potential. The solid lines are a least-squares fit to Eq. 6.

region of Fig. 3 after dividing by the appropriate steady-state current efficiency from Fig. 4b. Figure 5a is a plot of the steady-state stress as a function of the deposition potential for two independent data sets. The dashed black line is simply a guide for the eye. The deposits were limited to a nominal thickness of 50 nm. The growth stress is tensile over the entire range of potentials examined, varying from 100 MPa at more positive potential to a maximum of 800 MPa at more cathodic potentials. The agreement between the two data sets is fairly good.

Figure 5b is a plot of the steady-state stress as a function of the growth rate. Included in this plot are the two data sets plotted in Fig. 5a (red and blue points) as well as an additional data set (green) from a dual-pulse measurement which will be discussed later. The growth rate was obtained from the following expression:

$$R = \frac{\nu i M}{F n \rho} \quad [5]$$

where $\boldsymbol{R}$ is the growth rate, $\boldsymbol{\nu}$ is the steady-state current efficiency obtained from Fig. 4b, $\boldsymbol{F}$ is the Faraday constant, $\boldsymbol{n}$, $\boldsymbol{M}$ and $\boldsymbol{\rho}$ are the valency, atomic weight, and density, respectively, of Co, and $\boldsymbol{i}$ is the average current density measured over the last 5 nm of deposition.

The growth rate dependence in Fig. 5b is very similar to that reported for electrodeposited Cu and Ni.[37–39] The stress tends toward compressive at low growth rate and becomes more tensile as the growth rate increases. The tensile stress appears to saturate at a maximum value in the range of 700–800 MPa at the highest growth rate. As mentioned in the introduction, Chason has developed a model that captures the rate dependence of the steady-state stress as a balance between tensile stress due to grain coalescence and compressive stress due to insertion of atoms into the grain boundary. This balance depends on the specific growth parameters:[37–39]

$$\sigma_{ss} = \sigma_C + (\sigma_T - \sigma_C)\, \exp\left(-\beta \frac{D}{RL}\right) \quad [6]$$

where $\boldsymbol{\sigma_C}$ is the compressive stress associated with adatom insertion into the grain boundary in response to the elevated surface chemical potential during deposition, $\boldsymbol{\sigma_T}$ is the tensile stress due to grain coalescence (inversely proportional to $\boldsymbol{L}^{1/2}$), $\boldsymbol{\beta}$ is a dimensionless material dependent parameter, $\boldsymbol{D}$ is an effective diffusivity between adatoms on

Downloaded on 2019-01-15 to IP 108.31.232.242 address. Redistribution subject to ECS terms of use (see ecsdl.org/site/terms_use) unless CC License in place (see abstract).

Table I. Average grain size of Co electrodeposits as determined from SEM micrographs of the as-deposited surface, based on at least 75 measurements. The thickness was calculated from the charge, corrected by the Co current efficiency. The growth rate was calculated using Eq. 5.

Potential) (V)	Current Density (mA/cm^2)	Growth Rate (nm/s)	Deposit Thickness (nm)	Grain Size (nm)
−1.190	−0.50	0.13	58	241 ± 55
−1.200	−1.23	0.35	148	241 ± 52
−1.225	−1.90	0.57	183	222 ± 49
−1.300	−4.29	1.36	267	185 ± 40

the free surface and the grain boundary, R is the growth rate and L is the grain size. Eq. 6 predicts that the steady-state stress depends exponentially on the dimensionless factor D/RL. The stress is expected to be compressive when $D/RL \gg 1$, i.e., under conditions where atoms are able to diffuse into the grain boundary. Alternatively, the stress is tensile when $D/RL \ll 1$, i.e., when the deposition rate is large relative to the rate of diffusion of atoms into the grain boundary. The solid lines in Fig. 5b represent the least squares fit of the two data sets to Eq. 6 with parameters $\sigma_C = -15$ MPa, $\sigma_T = 915$ MPa, and $\beta D/L = 0.2$ nm/s.

As seen in Eq. 6, the microstructure of the deposit has a direct impact on the stress evolution through the grain size and shape. Low mobility materials such as the Fe-group metals tend to develop columnar grain structures that do not increase significantly in size with thickness when deposited at low temperatures. In the present Co case, the stability of the stress-thickness at open circuit (Fig. 2b) and the fact that the stress-thickness vs. thickness curves generated during deposition and subsequent dissolution are nearly identical (Fig. S2) suggests that the grain size is stable and does not change with time during deposition. However, the chronoamperometry in Fig. 2a suggests that the initial density of Co nuclei, or more accurately their diffusion zones, increases with more negative deposition potential, suggesting that the grain size may have a dependence on potential.

In order to address these microstructural issues, selected Co electrodeposits were examined by X-ray diffraction. Figure S3(a) of the Supporting Information shows X-ray diffraction patterns for the evaporated Au substrate and three Co films electrodeposited over a range of potentials. As mentioned previously, the Au has a strong (111) crystallographic texture. The Co electrodeposits have the expected hexagonal close-packed (hcp) structure with a preferred basal plane orientation as evidenced by the strong 002 reflection. A strong basal plane orientation might suggest the possibility of large misfit stress in the Co; however, scanning tunneling microscopy studies show that Co electrodeposited onto Au (111) single crystals tends to adopt a lattice spacing that is closer to that of bulk Co rather than Au, clearly indicating a lack of registry with the substrate.[57–59] Although the Au substrate could induce some positive strain in the initial Co layers, the strain would be progressively reduced as the film thickens and make little contribution to the steady state stress observed in our Co films.

In an effort to quantify the grain size, the as-deposited surfaces of several Co electrodeposits were examined by SEM. An example of a typical deposit surface is shown in Figure S3(b) of the Supporting Information. All of the deposits examined were quite dense and had a nodular appearance. The results of the SEM analysis are shown in Table I along with selected deposition parameters. The deposit thicknesses vary somewhat but all are less than 300 nm which makes them relevant for this stress discussion. The fact that two films deposited at similar potential (−1.19 V and −1.20 V) have identical grain size even though the thicknesses vary by nearly a factor of 3 suggests that the grains are indeed columnar and have uniform size throughout the thickness. However, as the deposition potential is made more negative, the grain size decreases by about 20% over the range of potentials examined, ranging from 240 nm at the more positive potentials down to 185 nm at the more negative potentials. Inserting the average value for the grain size into $\beta D/L = 0.2$ nm/s from the least square fit above, the result is $\beta D = 44 \pm 6$ nm^2/s where the uncertainty in βD considers the variation of grain size with overpotential. Alternatively, if the data are fit to the model using the measured values of the grain size for L and interpolating when necessary, the quality of the fit is equally good, and the parameters are similar. The significance of βD and the value obtained from the model fit will be discussed later.

Dual-pulse deposition.—The expression in Eq. 6 applies to the steady-state region of the stress-thickness vs. thickness curves. Although the linear curves in Fig. 3 as well as the EQCM data, suggest steady-state growth, the deposition current in Fig. 2a does not. In order to address this discrepancy, as well as the apparent sluggish deposition at the more positive potentials, a nucleation step is inserted into the process. The cantilever was first equilibrated at a potential of −0.6 V. The potential was then stepped to −1.30 V to form a consistent 15 nm thick starting layer. The potential was then stepped to the desired growth potential for a total thickness of about 100 nm. Following deposition, the electrode was equilibrated at open circuit and the deposit was stripped as before. Figure 6a shows the current response for selected deposition potentials. The inset highlights the early stage of deposition. The current is identical for all of the deposits during the nucleation step. The current then responds in a manner that reflects the chosen growth potential. All of the deposition currents reach steady state. The stripping current magnitude and shape are similar to the single pulse transients shown in Fig. 2a except that the peak heights (and charge) are fairly uniform for all potentials. As a consequence, the average current efficiency calculated from the ratio of the anodic dissolution charge to the total cathodic charge is very similar to the steady-state EQCM values shown in Fig 4b. The nucleation step eliminates the sluggish behavior observed at the more positive potentials where the parasitic reaction is the primary reaction and possibly suppresses any pH increase at the electrode surface, thus preventing $Co(OH)_2$ precipitation. Interestingly, the stripping peak for the −1.19 V deposit in Fig. 6a does not show the second peak attributed to $Co(OH)_2$.

The stress-thickness vs. nominal thickness plots obtained from this dual pulse deposition is shown in Figure 6b. As expected, all of the deposits have an identical stress response for the nucleation step. When the potential is stepped to the corresponding growth potential, the stress-thickness reaches a new steady state rather quickly. As in the single pulse experiment, the curves become linear with slopes that increase as the deposition potential is made more negative. The steady-state stress was calculated from the slope of the stress-thickness vs. thickness curve over the final 10 nm of deposition, again considering the current efficiency that was determined from the stripping voltammetry. These steady-state stress values are also plotted as a function of growth rate in Fig. 5b along with the two sets of 50 nm thick single pulse data. The solid line represents a least square fit to Eq. 6 with parameters $\sigma_T = 775$ MPa, and $\beta D/L = 0.2$ nm/s. The nucleation pulse eliminates the sluggish deposition behavior observed at positive deposition potential for the single pulse deposits. As a consequence, the dual pulse data set lacks points in the low growth rate region. For this reason, σ_C was fixed at −15 MPa, the same value of σ_C that was obtained from the fit of the 50 nm data.

Discussion.—The shape of the stress curve and the fitting parameters for the 100 nm thick dual pulse data are consistent with those of the 50 nm single pulse. Although the smaller value of σ_T for the dual pulse data may suggest that the dual-pulse 100 nm films have a larger grain size than the single 50 nm films, the smaller steady-state stress may simply be a consequence of growing thicker films, particularly those grown at high growth rate as illustrated in the stress-thickness vs. thickness curves in Fig. 6b. The curves are fairly linear for deposition potentials more positive than −1.30 V; however, the curve at −1.325 V clearly shows a slope that decreases with deposit thickness. This downward trend is more dramatic at more negative potentials (not shown) which results in a decreased steady-state stress at higher growth rates. For this reason, the dual pulse data was limited

Downloaded on 2019-01-15 to IP 108.31.232.242 address. Redistribution subject to ECS terms of use (see ecsdl.org/site/terms_use) unless CC License in place (see abstract).

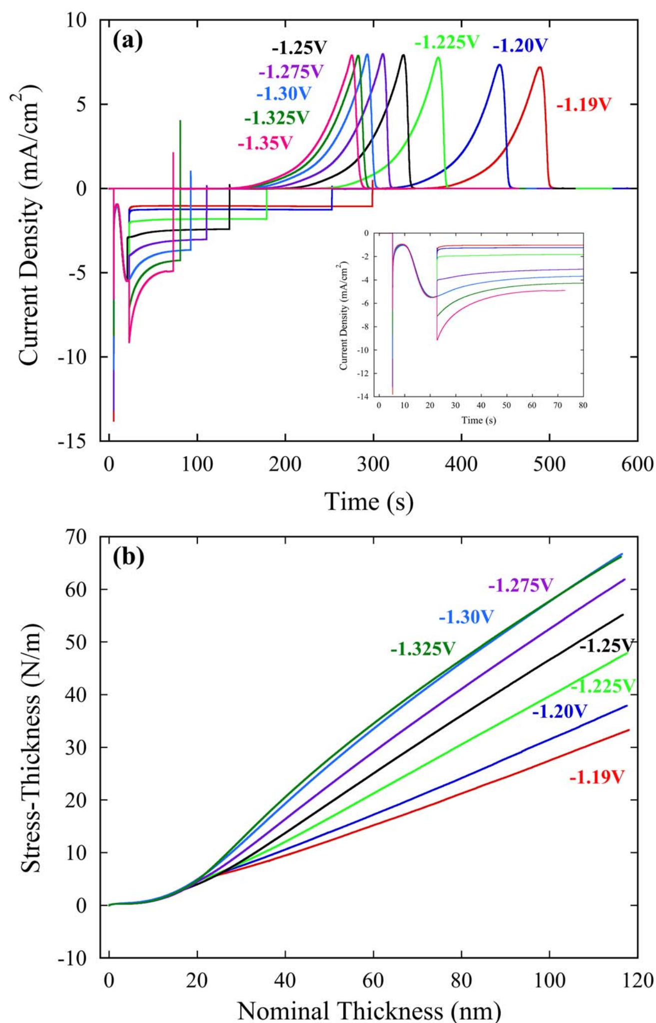

Figure 6. (a) Chronoamperometry and (b) stress-thickness response for Co electrodeposition onto an Au cantilever electrode in 0.1 mol/L $CoSO_4$ + 0.5 mol/L H_3BO_3 + 0.5 mol/L Na_2SO_4 (pH 4.5). The potential was stepped from −0.6 V to −1.3 V to nucleate a 15 nm thick layer, then stepped to the deposition potential of interest for a nominal deposit thickness of 100 nm while the cantilever deflection was monitored by the PSD. Following deposition, the electrode was allowed to equilibrate at the open circuit potential (≈ -1.05 V) for 10 s, prior to initiating an anodic voltammetric sweep at 2 mV/s until the deposit was completely removed. The stripping potential was limited to −0.4V. The inset in (a) highlights the early stage of deposition.

to growth rates less than 1.15 nm/s. A slight negative curvature in the stress-thickness is also apparent at −1.40 V for the single pulse 50 nm film (Fig. 3). Because this negative curvature in the stress data is only observed at the more negative potentials (high growth rate), our current speculation is that this behavior is due to surface roughness and not an increase in grain size. It has been demonstrated that roughness has a direct influence on the cantilever sensitivity and that corrections to Stoney's equation are often necessary.[60] Although there are indications that roughness can also impact the coalescence-induced tensile stress during Volmer-Weber growth,[61,62] no clear picture has emerged that describes the impact of roughness on the overall steady-state stress of the film.

The range of steady-state stress observed in these Co electrodeposits is approximately 100 to 800 MPa and is observed over a relatively small range of growth rates, less than 2.5 nm/s. In contrast, the range of steady-state stress for electrodeposited Cu and Ni is reported to be −60 to +60 MPa[38] and −600 to +400 MPa[18,37] respectively, for a considerably larger range of growth rates. The disparity in the growth rates simply reflects the concentration of the electroactive metal ions in solution, 0.7 mol/L and 1.36 mol/L for Cu and Ni respectively, compared to 0.1 mol/L for Co. Larger growth rates for Co deposition are clearly accessible from more concentrated Co^{2+} electrolytes, but the complications associated with $Co(OH)_2$ precipitation are more likely at the higher concentration, particularly when examining the lower growth rates. The large tensile stresses associated with Co deposition are also consistent with the kinetic parameters obtained from fitting the experimental data to Eq. 6. Our 44 nm^2/s value for $\boldsymbol{\beta D}$ is considerably less than the reported values of 1600 nm^2/s and 800 nm^2/s for Cu and Ni. The larger values of $\boldsymbol{\beta D}$ for Cu and Ni indicate that the ad-atom insertion mechanism is quite active and that the transition from compressive stress to tensile stress extends out to larger growth rates. This stress transition occurs at about 2 nm/s for Cu and 1 nm/s for Ni. No compressive to tensile transition was observed for Co at the growth rates and film thicknesses examined here. Extrapolation of the available data places the transition at about 0.05 nm/s. The fact that the steady-state stress for Co varies from 100 to 800 MPa with growth rate certainly indicates that ad-atom insertion into the grain boundary is an active stress generating mechanism. However, the extremely low value for $\boldsymbol{\beta D}$, at least for the deposition conditions examined here, further indicates that it only relieves the coalescence-induced tensile stress at extremely low growth rates.

Growth rate is only one of several processing variables that can be used to control the steady-state stress of an electrodeposit. Because deposit microstructure is critical to the growth rate dependence, any number of potential pulsing schemes (direct pulse, reverse pulse) can be expected to influence the final stress state through control of the grain size. Pulsed deposition also allows for stress relaxation during the off-pulse, if such relaxation mechanisms are operative[43,63], although little structural relaxation was seen in the electrodeposited Co examined here. The most direct approach for stress mitigation is through the use of chemical additives. The addition of saccharine is known to significantly reduce the tensile stress in Ni electrodeposits. Although additives can influence the stress due to grain refinement, evidence suggests that saccharine addition might alter the energetics of nuclei coalescence.[64,65] Thus, the influence of chemical additives on the growth stress of electrodeposited Co will be the focus of future work.

Conclusions

In situ cantilever curvature is used to quantify the growth stress in Co thin films electrodeposited from an electrolyte consisting of 0.5 mol/L Na_2SO_4, 0.5 mol/L H_3BO_3, and 0.1 mol/L $CoSO_4 \cdot 7\ H_20$. Stress-thickness (the average biaxial film stress multiplied by the thickness of the film) vs. thickness curves are measured as a function of the deposition potential, and the steady-state stress is obtained from their slopes, which in turn, is examined as a function of growth rate. Stresses as low as +85 MPa (tensile) are obtained at small growth rate, increasing to a limiting value of 800 MPa as the growth rate increases. The data is fit to Chason's kinetic model[42] that treats the stress as a dynamic competition between coalescence-induced tensile stress and compressive stress due to insertion of atoms into the grain boundary. Kinetic parameters for Co indicate that stress development is dominated by nuclei coalescence and that ad-atom insertion into the grain boundary contributes to the overall stress only at very low growth rates.

Acknowledgment

The authors gratefully acknowledge Carlos Beauchamp and Maureen Williams for technical contributions. Cantilever metallization by electron beam evaporation was performed at the Center for Nanoscale Science and Technology NanoFab at the National Institute of Standards and Technology.

ORCID

G. R. Stafford https://orcid.org/0000-0003-3445-9402

Downloaded on 2019-01-15 to IP 108.31.232.242 address. Redistribution subject to ECS terms of use (see ecsdl.org/site/terms_use) unless CC License in place (see abstract).

References

1. J. L. Bubendorff, E. Beaurepaire, C. Mény, and J. P. Bucher, *Journal of Applied Physics*, **83**(11), 7043 (1998).
2. J. García-Torres, E. Gómez, and E. Vallés, *Journal of Applied Electrochemistry*, **39**(2), 233 (2008).
3. P. Prod'homme, F. Maroun, R. Cortès, P. Allongue, J. Hamrle, J. Ferré, J. P. Jamet, and N. Vernier, *Journal of Magnetism and Magnetic Materials*, **315**(1), 26 (2007).
4. M. Gauvin, N. L. Yang, Z. J. Yang, I. Arfaoui, and M. P. Pileni, *Nano Res*, **8**(11), 3480 (2015).
5. M. Hagarova, D. Jakubeczyova, and J. Cervova, *International Journal of Electrochemical Science*, **10**(12), 9968 (2015).
6. C. Quan and Y. D. He, *Applied Surface Science*, **353**, 1320 (2015).
7. M. De Koninck, S.-C. Poirier, and B. Marsan, *Journal of The Electrochemical Society*, **154**(4), A381 (2007).
8. Y. Liang, H. Wang, P. Diao, W. Chang, G. Hong, Y. Li, M. Gong, L. Xie, J. Zhou, J. Wang, T. Z. Regier, F. Wei, and H. Dai, *Journal of the American Chemical Society*, **134**(38), 15849 (2012).
9. Y. Y. Liang, Y. G. Li, H. L. Wang, J. G. Zhou, J. Wang, T. Regier, and H. J. Dai, *Nat Mater*, **10**(10), 780 (2011).
10. H. Wang, Y. Liang, Y. Li, and H. Dai, *Angewandte Chemie International Edition*, **50**(46), 10969 (2011).
11. V. M. Dubin, R. Akolkar, C. C. Cheng, R. Chebiam, A. Fajardo, and F. Gstrein, *Electrochimica Acta*, **52**, 2891 (2007).
12. M. H. v. d. Veen, K. Vandersmissen, D. Dictus, S. Demuynck, R. Liu, X. Bin, P. Nalla, A. Lesniewska, L. Hall, and K. Croes, *in* "*2015 IEEE Mater. Adv. Metallization Conf.*", p. 25, 2015.
13. A. A. Vyas, C. J. Zhou, and C. Y. Yang, *Ieee Transactions on Nanotechnology*, **17**(1), 4 (2018).
14. D. Josell, M. Silva, and T. P. Moffat, *Journal of the Electrochemical Society*, **163**(14), D809 (2016).
15. C. H. Lee, J. E. Bonevich, J. E. Davies, and T. P. Moffat, *Journal of the Electrochemical Society*, **156**(8), D301 (2009).
16. R. Abermann, *Vacuum*, **41**, 1279 (1990).
17. J. A. Floro, E. Chason, R. C. Cammarata, and D. J. Srolovitz, *MRS Bulletin*, **27**(01), 19 (2002).
18. S. J. Hearne and J. A. Floro, *J. Appl. Phys.*, **97**, 014901 (2005).
19. S. J. Hearne, S. C. Seel, J. A. Floro, C. W. Dyck, W. Fan, and S. R. J. Brueck, *J. Appl. Phys.*, **97**, 083530 (2005).
20. R. W. Hoffman, *Thin Solid Films*, **34**, 185 (1976).
21. R. Koch, *J. Phys.: Condensed Matter*, **6**, 9519 (1994).
22. W. D. Nix and B. M. Clemens, *J. Mater. Res.*, **14**, 3467 (1999).
23. F. Spaepen, *Acta Mater*., **48**, 31 (2000).
24. R. J. Gleixner and W. D. Nix, *Journal of Applied Physics*, **86**(4), 1932 (1999).
25. O. E. Kongstein, U. Bertocci, and G. R. Stafford, *J. Electrochem. Soc.*, **152**, C116 (2005).
26. L. B. Freund and E. Chason, *Journal of Applied Physics*, **89**(9), 4866 (2001).
27. A. Rajamani, B. W. Sheldon, E. Chason, and A. F. Bower, *Appl Phys Lett*, **81**(7), 1204 (2002).
28. J. S. Tello, A. F. Bower, E. Chason, and B. W. Sheldon, *Physical Review Letters*, **98**(21), (2007).
29. R. C. Cammarata, T. M. Trimble, and D. J. Srolovitz, *Journal of Materials Research*, **15**(11), 2468 (2000).
30. E. Chason, B. W. Sheldon, L. B. Freund, J. A. Floro, and S. J. Hearne, *Physical Review Letters*, **88**(15), 156103 (2002).
31. C. Friesen, S. C. Seel, and C. V. Thompson, *J. Appl. Phys.*, **95**, 1011 (2004).
32. R. Koch, D. Hu, and A. K. Das, *Physical Review Letters*, **94**(14), 146101 (2005).
33. J. W. Shin and E. Chason, *Phys. Rev. Lett.*, **103**, 056102 (2009).
34. M. J. Buehler, A. Hartmaier, and H. J. Gao, *J Mech Phys Solids*, **51**(11-12), 2105 (2003).
35. C.-W. Pao, S. M. Foiles, E. B. Webb, D. J. Srolovitz, and J. A. Floro, *Physical Review Letters*, **99**(3), 036102 (2007).
36. A. Saedi and M. J. Rost, *Nat Commun*, **7**, (2016).
37. E. Chason, *Thin Solid Films*, **526**, 1 (2012).
38. E. Chason, A. Engwall, F. Pei, M. Lafouresse, U. Bertocci, G. Stafford, J. A. Murphy, C. Lenihan, and D. N. Buckley, *Journal of The Electrochemical Society*, **160**(12), D3285 (2013).
39. E. Chason, J. W. Shin, S. J. Hearne, and L. B. Freund, *Journal of Applied Physics*, **111**(8), (2012).
40. J. Murphy, C. Lenihan, M. Rybalchenko, N. Quill, A. Bourke, M. O'Grady, R. Lynch, and D. N. Buckley, *ECS Transactions*., **85**, 1071 (2018).
41. E. Chason, A. M. Engwall, Z. Rao, and T. Nishimura, *Journal of Applied Physics*, **123**(18), (2018).
42. A. M. Engwall, Z. Rao, and E. Chason, *Mater Design*, **110**, 616 (2016).
43. A. M. Engwall, Z. Rao, and E. Chason, *Journal of the Electrochemical Society*, **164**(13), D828 (2017).
44. T. Z. Luo, L. Guo, and R. C. Cammarata, *J. Crystal Growth*, **312**, 1267 (2010).
45. M. Fayette, U. Bertocci, and G. R. Stafford, *Journal of the Electrochemical Society*, **163**(5), D146 (2016).
46. G. R. Stafford and U. Bertocci, *J. Phys. Chem. B*, **110**, 15493 (2006).
47. G. G. Stoney, *The Tension of Metallic Films Deposited by Electrolysis*, 172 (1909).
48. M. Fleischmann and A. Saraby-Reintjes, *Electrochimica Acta*, **29**, 69 (1984).
49. H. Ibach, *Journal of Vacuum Science Technology A*, **12**(4), 2240 (1994).
50. D. R. Lide, *CRC Handbook of Chemistry and Physics.*, 86th ed., (2005).
51. H. Deligianni and L. T. Romankiw, *Ibm J Res Dev*, **37**(2), 85 (1993).
52. J. Ji, W. C. Cooper, D. B. Dreisinger, and E. Peters, *Journal of Applied Electrochemistry*, **25**(7), 642 (1995).
53. N. L. Ritzert and T. P. Moffat, *Journal of Physical Chemistry C*, **120**(48), 27478 (2016).
54. P. Vereecken, *Personal Communication*, 230th Meeting of the Electrochemical Soc., Honolulu, HI, 2006.
55. B. Scharifker and G. Hills, *Electrochim. Acta*, **28**, 879 (1983).
56. J. S. Santos, R. Matos, F. Trivinho-Strixino, and E. C. Pereira, *Electrochimica Acta*, **53**(2), 644 (2007).
57. P. Allongue, L. Cagnon, C. Gomes, A. Gündel, and V. Costa, *Surface Science*, **557**(1-3), 41 (2004).
58. L. Cagnon, A. Gundel, T. Devolder, A. Morrone, C. Chappert, J. E. Schmidt, and P. Allongue, *Applied Surface Science*, **164**(1–4), 22 (2000).
59. M. Kleinert, H. F. Waibel, G. E. Engelmann, H. Martin, and D. M. Kolb, *Electrochimica Acta*, **46**(20–21), 3129 (2001).
60. J. Weissmuller and H. L. Duan, *Physical Review Letters*, **101**(14), (2008).
61. B. W. Sheldon, K. H. A. Lau, and A. Rajamani, *Journal of Applied Physics*, **90**(10), 5097 (2001).
62. L. A. Zepeda-Ruiz, E. Chason, G. H. Gilmer, Y. M. Wang, H. W. Xu, A. Nikroo, and A. V. Hamza, *Appl Phys Lett*, **95**(15), (2009).
63. D. Xu, V. Sriram, V. Ozolins, J. M. Yang, K. N. Tu, G. R. Stafford, and C. Beauchamp, *Journal of Applied Physics*, **105**(2), 023521 (2009).
64. A. Bhandari, S. J. Hearne, B. W. Sheldon, and S. K. Soni, *J. Electrochem. Soc.*, **156**, D279 (2009).
65. S. R. Brankovic, B. Kagajwala, J. George, G. Majkic, G. Stafford, and P. Ruchhoeft, *Electrochimica Acta*, **83**, 387 (2012).

Downloaded on 2019-01-15 to IP 108.31.232.242 address. Redistribution subject to ECS terms of use (see ecsdl.org/site/terms_use) unless CC License in place (see abstract).